Chapter 7

Calorimetry

The final measurement technique that is in general use in particle physics experiments is *calorimetry*: as its name indicates, this consists in total absorption of both charged and neutral particles (in practice, besides neutrinos, in high-energy experiments only muons typically pass all the way through a calorimeter and only suffer ionization energy losses), and a measurement of their energies.

The topic of calorimetry can be divided into two classes: electromagnetic and hadronic calorimetry. The first deals largely with the interactions of electrons, positrons, and photons: this is a very limited set of particles, but they often have particular importance in the experiments; and their interactions with the detector materials are such that a particularly good energy resolution can be achieved.

Interactions of hadrons with calorimeter materials are much more complicated, typically involving the strong interaction between the incident hadron and the nuclei of the detector matter.

There are many good texts on various aspects of calorimetry. For a comprehensive review of the topic, see *e.g.* the book by Wigmans [1].

7.1 Electromagnetic Calorimetry

The interactions of electrons and photons with detector materials have been computed exactly. For low-energy electrons (and positrons), the same ionization energy loss mechanism is relevant as for general charged particles (see Chapter 3). However, for high energies, other mechanisms degrading the energies of incident particles become important. These are described in the Section 7.1.1, followed by a description of the macroscopic picture of an EM *shower*, and the methods used to convert the resulting signal into an electronics signal.

A semi-classical derivation of the energy loss mechanism for electrons and positrons can be found in Chapter 15 of the book by Jackson [2].

7.1.1 Interaction of electrons and photons

Bremsstrahlung

The discussion of the energy loss mechanism for ultra-relativistic electron starts from the notion that *any accelerated charged particle emits radiation.* In particular, we consider here the acceleration of particles due to collisions with detector materials. Here we will only describe qualitatively the features of the emitted radiation, in this context called *bremsstrahlung*:

- the description of the acceleration undergone by the incident particle is (for small scattering angles) essentially given by the Rutherford scattering formula in Section 3.3;
- this formula can be linked to that giving the intensity of the emitted radiation as a function of the acceleration of the incident particle (or equivalently, its momentum transfer). In principle, both the incident particle and the matter particle are accelerated; but the collision with atomic nuclei in particular (with in general large masses) will lead to acceleration of, and hence radiation by, essentially the incident particle only.

  As the momentum transfer, and hence the acceleration, is proportional to the charge of the scattering nucleus, the emitted radiation will be proportional to the square of this charge (in contrast to ionization energy loss, in which this dependence is approximately linear). Alse, the scattering off the atomic electrons can be neglected (as in the discussion of multiple Coulomb scattering);
- it turns out that the momentum dependences of the two formulae involved conspire to leave a factor m^{-2} in the result for the radiation intensity. It is for this reason that bremsstrahlung typically plays an important role only for electrons and positrons.

This process has also been computed quantum-mechanically in 1934 by Bethe and Heitler, in the limit of an infinitely heavy, pointlike, spinless nucleus. Graphically, it is represented by the Feynman diagrams of Figure 7.1. It can be seen that the process is much like the fundamental vertex of QED,

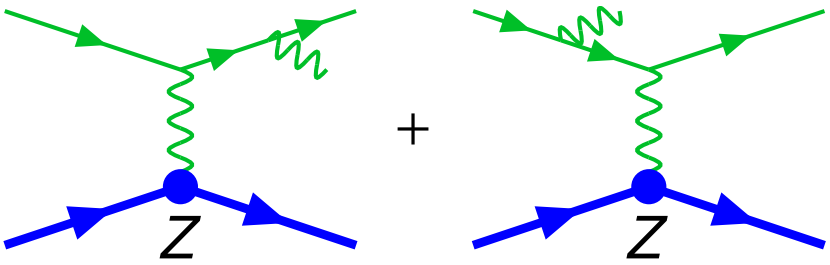

Figure 7.1: Feynman diagrams for bremsstrahlung

coupling electrons (and/or positrons) to photons. Kinematics forbids the emission of a photon by an electron moving in vacuum; however, in the presence of matter, the "external" Coulomb field of the nucleus provides additional four-momentum and the emission can take place. The situation is complicated by the fact that the Coulomb field of the nucleus is *screened* by the atomic electrons, again as for the case of multiple Coulomb scattering.

The result of the Bethe-Heitler calculations for the emission cross section is that for energies E and k of the incoming particle and the emitted photon, respectively, we have (for an exhaustive overview of the bremsstrahlung process, see *e.g.* the paper by Tsai [3]):

$$\frac{\mathrm{d}\sigma}{\mathrm{d}k} = \frac{4\sigma_0}{k}\left(\frac{4}{3}(1-k/E)+(k/E)^2\right)\ln(183Z^{-1/3}), \tag{7.1}$$

with

$$\sigma_0 = \alpha Z^2 r_\mathrm{e}^2 = \alpha Z^2\left(\frac{\hbar\alpha}{m_\mathrm{e}c}\right)^2. \tag{7.2}$$

This formula is valid for not too high values of Z. Besides the photon energy spectrum, also the photon *angular distribution* is an important parameter: for high energy electrons, the average photon emission angle with respect to the electron direction is $1/\gamma$, leading to a very collimated behaviour.

The total energy loss due to bremsstrahlung is obtained from Eqn. 7.1 simply by computing

$$-\frac{\mathrm{d}E}{\mathrm{d}x} = n_{\mathrm{A}} \int_{k=0}^{k_{\max}=E-m_{\mathrm{e}}\approx E} k \frac{\mathrm{d}\sigma}{\mathrm{d}k} \mathrm{d}k = 4 n_{\mathrm{A}} \sigma_0 \ln(183 Z^{-1/3}) E.$$

With the definition of the *radiation length* already seen in Chapter 3,

$$X_0^{-1} = 4\sigma_0 n_{\mathrm{A}} \ln(183 Z^{-1/3}),$$

we therefore have

$$-\frac{\mathrm{d}E}{\mathrm{d}x} = \frac{E}{X_0}.$$

Again, as stated in Chapter 3 as well, the inverse radiation length for a mixture of materials can be approximated as a weighted sum (by weight fraction) over the materials.

The preceding treatment ignores other energy loss mechanisms, which of course in reality take place as well. For reference, we show again in Figure 7.2 the complete energy loss curve already shown in Chapter 3 (but notice that that curve is made for *muons* rather than electrons!): Clearly at the

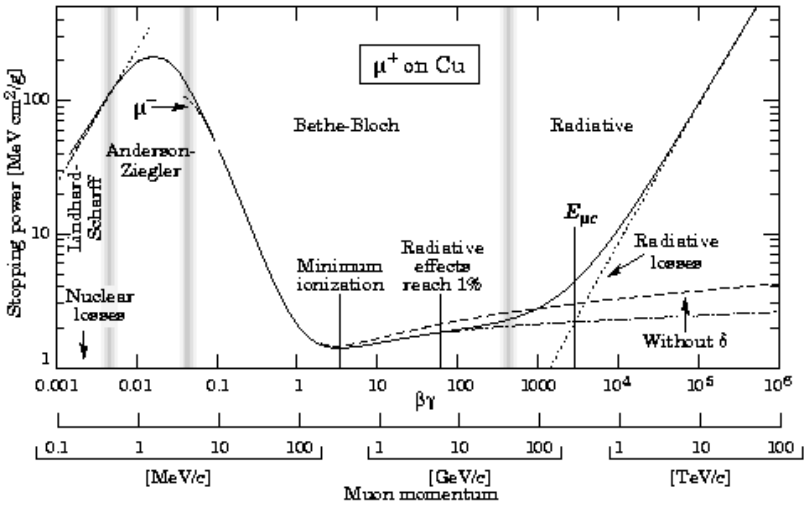

Figure 7.2: Energy loss by charged particles

energy scale where bremsstrahlung becomes relevant, it quickly becomes the dominant effect. The ratio of the energy loss of electrons due to bremsstrahlung and that due to collisions is roughly given by

$$\frac{ZE}{1.6 \cdot 10^3 m_{\mathrm{e}} c^2}.$$

Therefore, it is convenient to define a "critical energy" E_c, at which the two are equal:

$$E_c = \frac{1.6 \cdot 10^3}{Z} m_{\mathrm{e}} c^2.$$

To first order, all energy loss can be thought to be due to bremsstrahlung for energies $E > E_c$, and due to collisions for energies $E < E_c$. The critical energy depends quadratically on the mass of the radiating particle. Therefore, even for the next lightest particle, the muon, the bremsstrahlung process becomes important only at energies of the order of 500 GeV.

It may be noted that there is an alternative definition of the critical energy E_c, used *e.g.* by the Particle Data Group [4]: here, it is the defined as the energy of electrons and positrons at which their energy loss by collisions per radiation length equals their energy, *i.e.*

$$-\frac{\mathrm{d}E}{\mathrm{d}x} = \frac{E_c}{X_0}.$$

The difference between the two alternative definitions is small, and we will neglect it.

Pair creation

This is also an appropriate time to consider in some detail the interactions between photons and matter. We have already discussed the photoelectric effect in the context of photodetection. While for low energies a single electron is emitted, for higher energies the atom can end up in excited states and return to its ground state through the emission of X-ray photons or Auger electrons. In fact, this contribution dominates the total photon interaction cross-section for energies well above the eV level relevant for visible light: as can be seen in Figure 7.3 for the case of argon, this is true up to energies of about 500 keV. This limit can be as low as 20 keV (for *e.g.* C), or as high as 700 keV (for the heaviest element that can be used to construct calorimeters, U). The photoelectric effect clearly

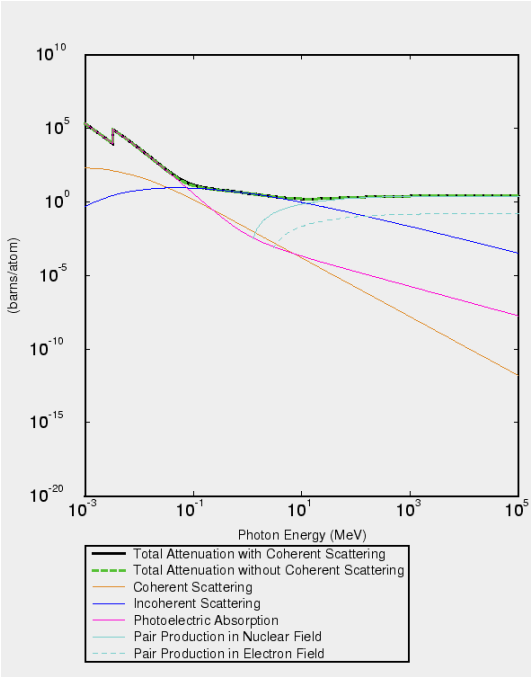

Figure 7.3: Total photon cross sections in argon

involves the atom as a whole; the cross section for this process is highly dependent on the number of atomic electrons, and therefore on the nucleus's value of Z: roughly between Z^4 and Z^5. The cross section depends on energy as E^{-3}.

Similarly, at low energies, photons suffer *Rayleigh scattering* (well-known for its effect on the sky). In this process, only the photon *direction* is changed, whereas its energy remains the same. As a consequence, Rayleigh scattering does not lead to an energy degradation of incoming photons, and therefore it is not of much relevance for calorimetry.

At higher energies, *Compton scattering* becomes important. Here, an incident photons scatters off an atomic electron with sufficient momentum (and energy) transfer to put the electron in an unbound state, and differs from the photoelectric effect in that the photon is not absorbed. This process is shown in Figure 7.4. Purely from the kinematics of the process (conservation of four-momentum), it

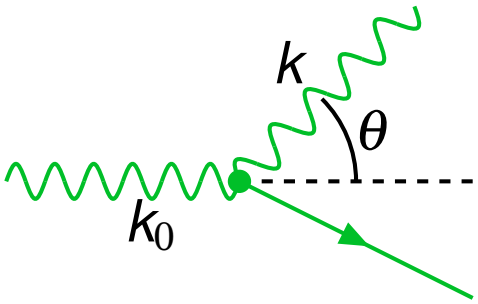

Figure 7.4: Compton scattering: kinematics

can be calculated that the energy and angle of the outgoing photon are related by

$$k = \frac{k_0 m_\mathrm{e}}{m_\mathrm{e} + k_0(1 - \cos\theta)}.$$

It was the experimental demonstration of this relation that definitively established the particle nature of the photon.

The Compton scattering cross section can be calculated in the framework of QED and is represented by the Feynman diagrams in Figure 7.5. The result is the *Klein-Nishina formula*:

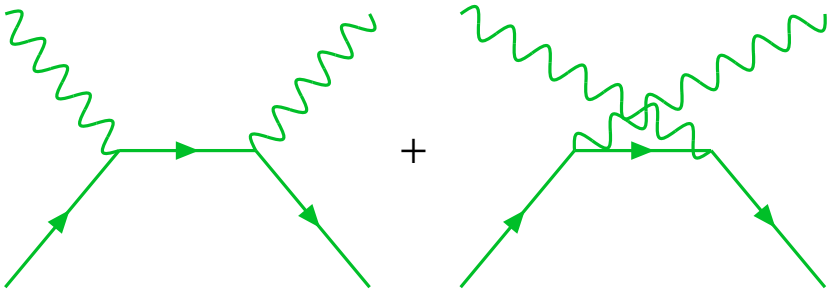

Figure 7.5: Feynman diagrams for Compton scattering

$$\frac{\mathrm{d}\sigma}{\mathrm{d}k} = \frac{\pi}{\varepsilon k}\left(\frac{\hbar\alpha}{m_\mathrm{e}c}\right)^2 \left(1 + (k/k_0)^2 - 2(\varepsilon+1)/\varepsilon^2 \cdot (k/k_0) + 1/\varepsilon^2 \cdot k_0/k\right)$$

with k_0 (k) the energy of the incoming (outgoing) photon, and

$$\varepsilon = \frac{k_0}{m_\mathrm{e}c^2}.$$

It is instructive to compute the integrated cross-section in the limits of small and large photon energies:

$$\begin{aligned} \varepsilon \ll 1 \quad \sigma &= \frac{8}{3}\pi\left(\frac{\hbar\alpha}{m_\mathrm{e}c}\right)^2 \equiv \sigma_\mathrm{Thomson}, \\ \varepsilon \gg 1 \quad \sigma &= \sigma_\mathrm{Thomson} \cdot \frac{3}{8\varepsilon}\left(\ln(2\varepsilon) + \frac{1}{2}\right). \end{aligned}$$

Of course, this is the cross-section *per electron*. To obtain the total cross-section for an atom, this has to be multiplied with its value of Z. The Compton scattering process is important for calorimetry to the extent that it is this process which is responsible for the final energy degradation to low-energy electrons.

The process that is of primary interest in the context of calorimetry is that of *pair production*, shown diagrammatically in Figure 7.6. This process is much like the bremsstrahlung process, in the

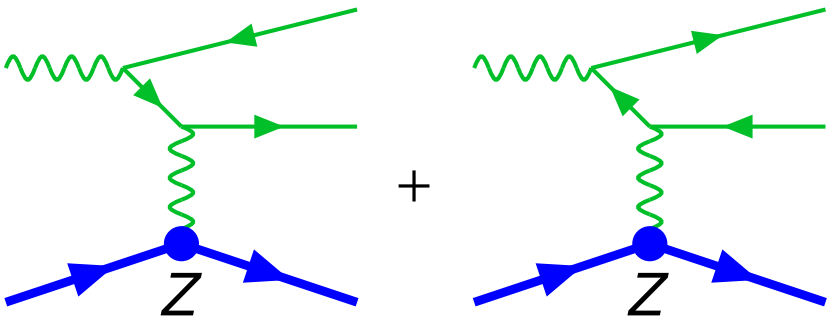

Figure 7.6: Feynman diagrams for pair production

sense that the presence of an "external" Coulomb field is required to provide the four-momentum necessary for the photon to "split" into an e^+e^- pair; two processes are in fact even more similar, as the diagram for pair creation can be obtained from that for bremsstrahlung by simply interchanging an electron and a photon line. In addition, screening of the atom's nucleus by its electrons again plays a role.

The pair creation process, too, was first calculated in the framework of QED by Bethe and Heitler, and the differential cross section for an incoming photon of energy k as a function of the energy of the positron, E, is given by [3]

$$\frac{\mathrm{d}\sigma}{\mathrm{d}E} = \frac{4\sigma_0}{k}\left((E/k)^2 + ((k-E)/k)^2 + \frac{2}{3}E(k-E)/k^2\right)\ln(183Z^{-1/3})$$

(which can be checked explicitly to be symmetric under the interchange of positron and electron energies). This can again be integrated to give

$$\sigma = \int_0^k \frac{\mathrm{d}\sigma}{\mathrm{d}E}\mathrm{d}E = 4\sigma_0\frac{7}{9}\ln(183Z^{-1/3}).$$

The quantity σ_0 is the same as that defined in Eqn. 7.2; therefore, also in this case we can make use of the concept of *radiation length*, and write

$$\sigma = \frac{7}{9}(n_\mathrm{A}X_0)^{-1}. \tag{7.3}$$

Now the concept of energy loss is not meaningful in this case, as the photon does not lose energy in this process but in fact is lost; but it can be interpreted as a *linear attenuation* process, in which the intensity of a photon beam is attenuated as

$$I = I_0 e^{-\mu x}, \quad \mu = \left(\frac{9}{7}X_0\right)^{-1}.$$

The angles under which the $e^\pm$ are emitted with respect to the direction of the incoming photon, are small: of the order of $m_\mathrm{e}c^2/k$.

7.1.2 Shower development

From the preceding Section, it is clear that the high-energy regime of the interactions of electrons and photons is dominated by bremsstrahlung and pair production processes, respectively. If we neglect the other interactions, a rather simple picture emerges: a high-energy electron decreases its energy by radiating a series of bremsstrahlung photons, the bremsstrahlung photons in turn are converted into (lower energy) e^+e^- pairs, *etc*. This cascade of particles, of ever lower energies, is called an (electromagnetic) *shower*.

Neglecting also the fact that the distribution of a parent particle's energy over its two daughter particles is in general unequal, and the fact that the characteristic length for photons differs from that for electrons by a factor 9/7, the picture can be simplified even more to that shown in Figure 7.7. The shower stops roughly when other energy loss mechanisms become more important than

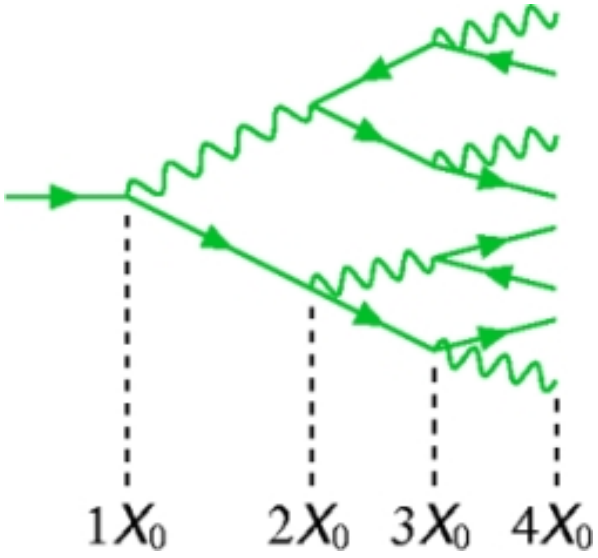

Figure 7.7: Simplified picture of an electromagnetic shower

the bremsstrahlung and pair production ones, *i.e.* at $E < E_c$. This leads to the following features:

- for a particle of initial energy E, the shower stops after $n = \ln(E/E_c)/\ln(2)$ steps, *i.e.* after a total depth $n \cdot X_0$ increasing logarithmically with energy;
- at this point the number of particles ($e^\pm$, γ) created in the shower is equal to E/E_c.

Note that the shower process itself essentially serves only to *stop* the incoming particle. The conversion of its energy into a measurable signal is a topic that will be addressed in the following Section; but essentially this relies on *other* energy loss mechanisms, in particular collision losses by electrons and positrons.

A more realistic approximation of the shower process has been made by Rossi [5]. This so-called "Approximation B" uses the expressions of Eqns. 7.1 and 7.3 for the bremsstrahlung and pair production processes, neglects Compton scattering, and treats energy loss due to collisions as independent of energy. This approximation allows to derive a parametrisation for the *longitudinal shower profile*, *i.e.* the total energy loss due to collisions as a function of shower depth. For an incident particle ($e^\pm$,

γ) of energy E, and with $t = x/X_0$:

$$\frac{\mathrm{d}E}{\mathrm{d}t} = E \cdot b(bt)^{a-1}e^{-bt}/\Gamma(a).$$

This parametrisation leads to a maximum at $t_{\max} = (a-1)/b$, with $b \approx 0.5$, and leads to a reasonable description of the data for showers beyond the first few radiation lengths if $t_{\max}$ is chosen appropriately:

$$t_{\max} = C + \ln(E/E_c), \tag{7.4}$$

with $C \approx -1$ for $e^{\pm}$ and $C \approx -0.4$ for photons. (To make it very clear: this means that as far as calorimetry is concerned, there is *very* little difference between electrons and photons!) An example is shown in Figure 7.8 for 2 GeV and 20 GeV incident electrons on blocks of copper ($Z = 29$) and lead ($Z = 82$). Note that while the shower appears to be somewhat longer in the higher-Z lead; however, it

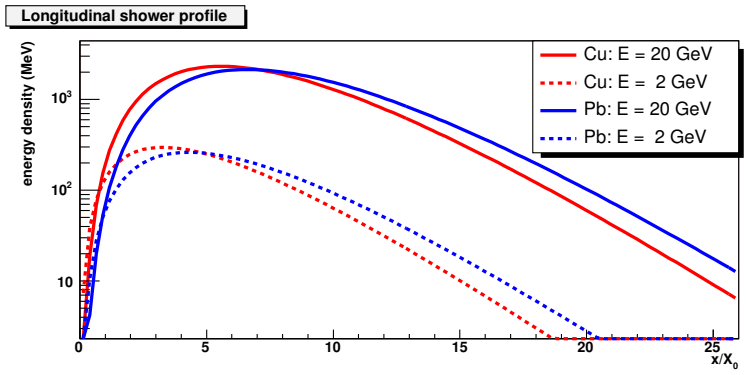

Figure 7.8: Longitudinal shower profile for electrons of 2 and 20 GeV energy in Cu and Pb

should be realized that the abscissa of this plot is *scaled* by X_0. This quantity scales roughly as $Z^{-2}A$, so that the shower in lead is much shorter!

The second general feature that one can deduce from this profile is that the amount of material required to fully contain a shower is substantial: of the order of 25–30 X_0 for showers initiated by particles of tens of GeV energy, corresponding to about 36 cm of Cu or 14 cm of Pb. As indicated by Eqn. 7.4, the calorimeter depth should scale logarithmically with energy to ensure longitudinal containment.

Notice that also this parametrisation is of limited validity, not only because it considers only the longitudinal profile (and neglects multiple scattering of electrons and positrons, leading to a finite shower width), but also because it neglects *fluctuations* in the shower process. It is not possible to take these into account analytically, but several computer codes using Monte Carlo methods exist. The best known is the EGS code. Example simulated showers (of a 1 GeV electron in 30 cm of Cu and Pb, respectively)are shown in Figure 7.9.

As said, Rossi's approximation ignores the lateral profile of the shower. The following effects lead to a broadening of the shower:

- multiple Coulomb scattering of the $e^{\pm}$;
- Compton scattering of the photons;
- the finite angles of daughter particles in bremsstrahlung and pair production processes.

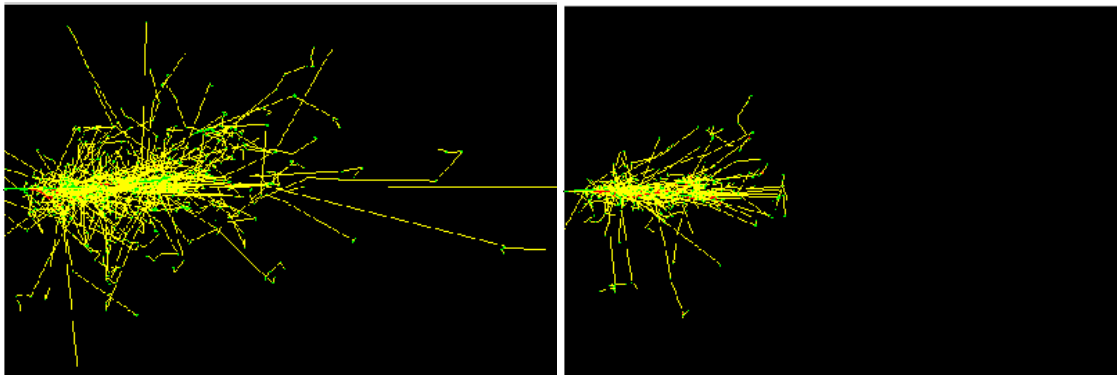

Figure 7.9: Showers due to 1 GeV incident electrons in Cu and Pb

At the start of the shower, its lateral extent is dominated by the last contribution, leading to a very narrow profile. However, as the energies of the particles involved decrease, multiple scattering becomes more and more important. As a consequence, the shower widens. The overall size of the shower is generally expressed in terms of the *Molière radius* R_{M}:

$$R_{\mathrm{M}} = \frac{E_s}{E_c} X_0 \approx \left(\frac{21.2\mathrm{MeV}}{E_c} \right) X_0.$$

In this formula, E_s is the same quantity already encountered in Chapter 3. The propagation of photons causes deviations from the scaling with R_{M}; however, about 95% of the shower is typically contained in a cylinder of radius $2R_{\mathrm{M}}$.

7.1.3 Detection

Our discussion so far has been restricted to the mechanism by which high energy electrons, positrons, and photons can be *absorbed* in calorimeter material. However, this is not the whole story: if the calorimeter is to be of use for the purpose of *energy measurement* of the incident particles, some mechanism is required to convert the deposited energy to a measurable electric signal.

As said in the previous Section, the "final" energy deposition is typically through collisions of low-energy electrons and positrons with the detector material. Three mechanisms can be exploited:

- ionization (we will return to this topic somewhat later, in the context of sampling calorimeters);
- Cherenkov radiation (even low-energy $e^{\pm}$ are relativistic due to the small mass of the electron!);
- and scintillation.

Independently of the precise mechanism, though, the produced signal is proportional to the total "track length" of $e^{\pm}$ in the material. Based on this notion, this total track length can be constructed in the following way:

1. using again the more simplistic picture of a shower, we assume that all particles *before* the last stage (at which the shower stops abruptly) travel a full radiation length, while particles at the last stage of the shower range out and travel a distance R;

2. with about 2/3 of the particles being electrons and positrons, the total track length becomes (for n stages)
$$T = X_0 \cdot \frac{2}{3}\sum_{j=0}^{n-1} 2^j + R \cdot \frac{2}{3}2^n = \frac{2}{3}(X_0 + R)2^n = \frac{2}{3}(X_0 + R)E/E_c;$$

3. in practice, there is often a detection threshold energy for charged particles, reducing the *visible track length*. However, this does not change the fact that the output signal (which we assume to be proportional to the visible track length) is still proportional to the energy of the incident particle.

Of course this linearity is maintained *only* if the full shower is contained in the calorimeter. Given that for higher energies of the incident particles the shower extends further, lack of (longitudinal) containment will introduce nonlinearities, particularly at the highest energies.

At this point it become useful to subdivide the possible EM calorimeters into two classes: *homogeneous* and *sampling* calorimeters.

Scintillating crystals

In homogeneous calorimeters, the absorber medium (degrading the energy of the incident particle through the EM shower) is at the same time the detection medium. With a few notable exceptions (which we will return to later), this combination can be achieved only if the detection occurs through the emission of (scintillation or Cherenkov) light, and hence the material of choice is typically a crystal.

In the case of *scintillation*, crystals are *anorganic* scintillators, as opposed to the organic scintillators discussed in Chapter 5. Here, the crystalline nature of the material leads to a band structure, and the principle of operation is that a traversing charged particle excites electrons from the valence band to the conduction band. This is followed by a decay back to the valence band, under emission of a photon. The principle is shown schematically in Figure 7.10. It turns out that except for a few

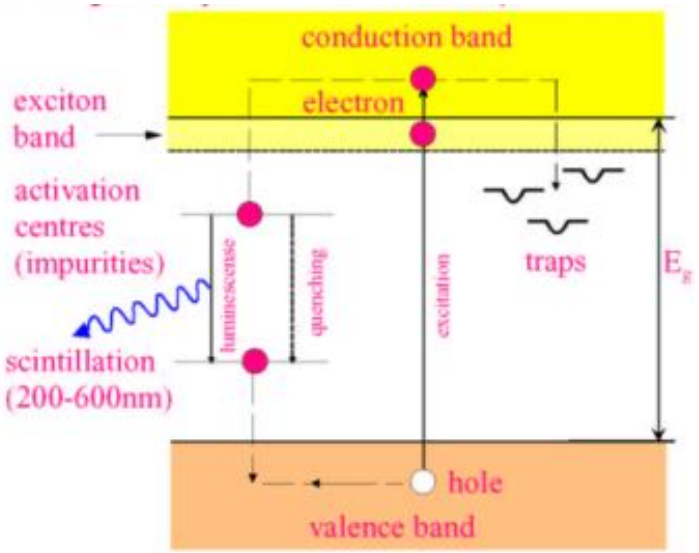

Figure 7.10: Operating principle of anorganic scintillators

materials (like $Bi_4Ge_3O_{12}$ or BGO, and BaF_2), this mechanism by itself is very inefficient. Therefore, in most cases impurities are introduced to create an "exciton" band between the valence and conduction bands. The impurity concentrations can typically be kept low, so that a good transparency of the crystal for the scintillation light is maintained. A good example is the widely used NaI(Tl), where a 0.1% thallium doping is adequate to serve as an "activator".

Compared to organic scintillators, anorganic scintillating crystals often have a higher light yield. However, the band structure does not offer the large amount of vibrational and rotational degrees of freedom that organic molecules have, and therefore the decay times for scintillators are usually significantly longer: as an example, the time constant for BGO is about 300 ns; in fact the decay in most crystals does not occur with a single time constant, but with two components having different constants. The wavelengths at which emission from the different components peaks also typically differ, but emission is typically at visible light frequencies (*e.g.* 480 nm for BGO).

In terms of speed, an exception is $PbWO_4$, which will be used in the electromagnetic calorimeter of the CMS experiment at the LHC: its slowest time constant (of 100 ns) contributes 1% to the total signal only, while fast time constants of 5 ns and 15 ns contribute 39% and 60%, respectively. This speed, in combination with good radiation hardness, makes this material appropriate for use in the LHC environment.

The light yield in scintillating crystals depends strongly on the material properties. For instance, they often have a strong temperature dependence, as shown in Figure 7.11. For instance, at room

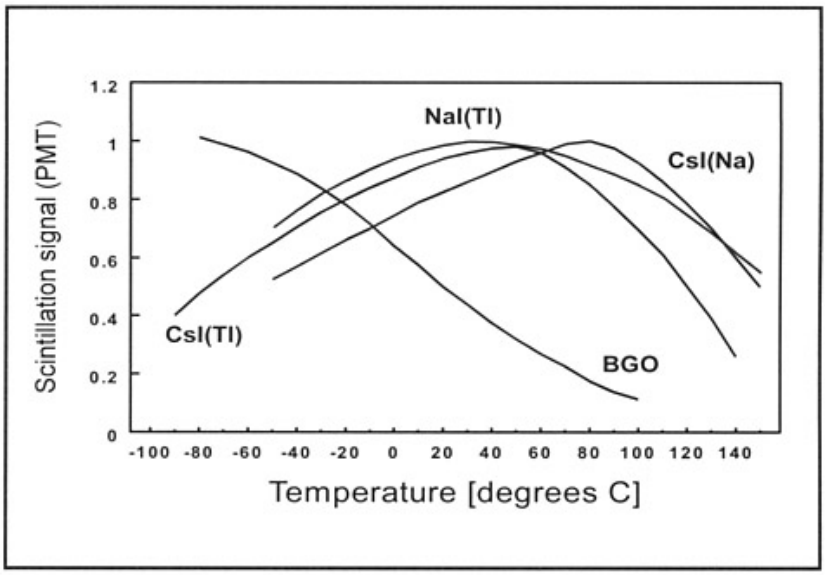

Fig. 3.3 ***Temperature dependence of the scintillation yield of NaI(Tl), CsI(Na), CsI(Tl) and BGO.***

Figure 7.11: Temperature dependence of the light yield of some anorganic scintillators

temperature, the light yield of BGO has a temperature dependence of -1.5%/K. In the case of the electromagnetic calorimeter of the L3 experiment, the temperature of the BGO crystals needed to be kept constant to within 0.2 K to ensure that temperature variations did not give an appreciable contribution to the total energy resolution.

While on the topic of energy resolution, it should be remarked that the fundamental contribution to the resolution is of *statistical* nature: to first order, in the case of scintillation, the number of

photoelectrons (for complete containment) obeys Poisson statistics. Therefore, for a given average number of photoelectrons n, the RMS spread around this average will be equal to $\sqrt{n}$. Given that the number of photoelectrons is proportional to the energy, it follows immediately that the corresponding contribution to the energy resolution will behave as

$$\frac{\sigma_E}{E} = \frac{a}{\sqrt{E}}.$$

In practice, the value of a is determined by the fluctuations in the charged track length as well as the photoelectron statistics; the corresponding contribution to the energy resolution is often called the *stochastic term*. This dependence is usually expressed by giving the term a in units of $(\text{GeV})^{1/2}$. Note that the relative precision of the energy measurement *improves* with energy, in marked contrast to the behaviour in *e.g.* tracking detectors!

When considering the total energy resolution, also other effects play a role:

- channel to channel variations: these are usually due to limited statistics available for the calibration of the calorimeter (relevant as the ultimate calibration is usually based on physics data). This leads to a resolution contribution that scales with the energy;
- electronics noise: this usually gives rise to a resolution contribution that is independent of energy.

As a result, the total resolution is usually parametrised as

$$\frac{\sigma_E}{E} = \frac{a}{\sqrt{E}} \oplus \frac{b}{E} \oplus c,$$

where the $\oplus$ denotes summing in quadrature.

As before, a way is needed to convert the light signal into an electric signal. Typically, calorimeter crystals are sizeable enough for their granularity to permit the use of PMTs; however, these tend to occupy a lot of space which is normally needed for hadronic calorimeters. Therefore, the more modern experiments have resorted to solid state photodetectors. Examples are:

- photodiodes (used *e.g.* in the EM calorimeter of the L3 experiment, shown in Figure 7.12). The

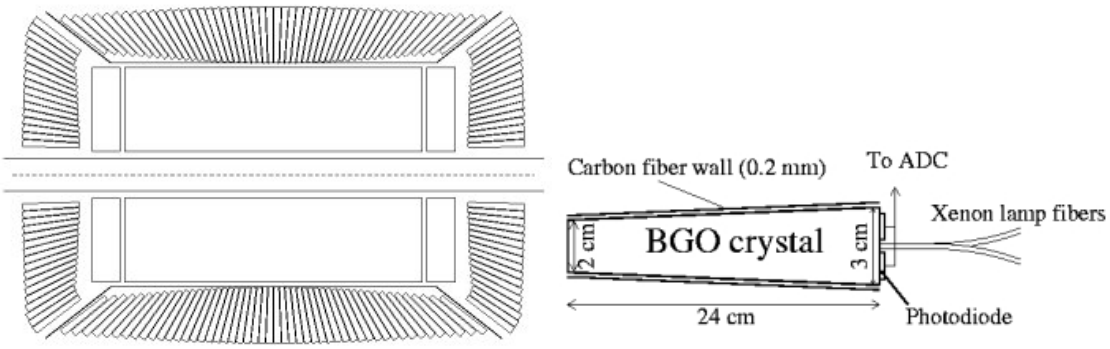

Figure 7.12: Layout of the EM calorimeter of the L3 experiment, comprising about 11,000 crystals, and of its crystals (including calibration instrumentation)

photodiode is essentially the same diode structure as the one encountered in charged particle

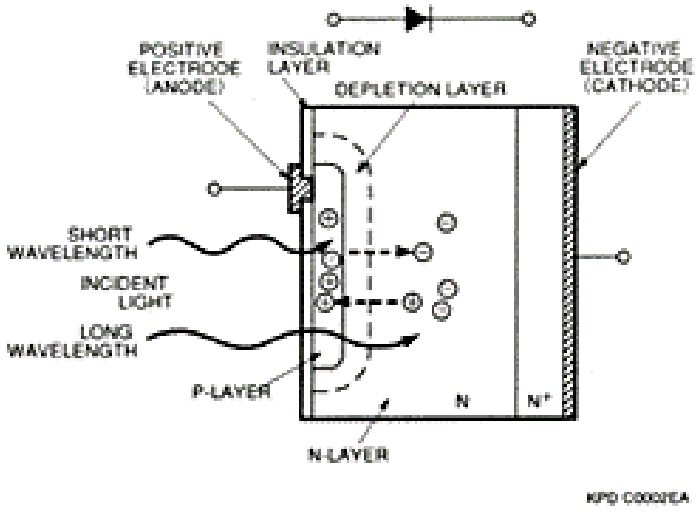

Figure 7.13: Operating principle of the photodiode

tracking using silicon devices; for completeness, its operating principle is shown in Figure 7.13. The quantum efficiency that can be obtained in this device is roughly 60–80%. In this device, no internal amplification of the signal takes place; therefore, to lead to a signal large enough to be fed into an electronics preamplifier the light yield of the crystal has to be relatively high. Fortunately, this is the case for the BGO crystals used: about 8200 photons per MeV of deposited energy.

The (energy dependence of the) resolution is eventually determined from physics data: L3 being located at an e^+e^- collider, the Bhabha scattering ($e^+e^- \to e^+e^-$) process, which (in the absence of significant radiative effects) can be used to calibrate the detector and determine its energy resolution. At lower energies, the production of known resonances can be used. The result is shown in Figure 7.14, and can be parametrised as

$$\frac{\sigma_E}{E} = \frac{2\%}{\sqrt{E}} \oplus 0.7\%.$$

Figure 7.15 shows how the calorimeter resolution is obtained from the reconstruction of known resonances, in this case through the decays $\pi^0 \to \gamma\gamma$ and $\eta \to \gamma\gamma$.

Besides the energy resolution, also the *position resolution* is an important parameter (although less crucial than the energy resolution). In the case of the L3 EM calorimeter, the crystals are tapered, with a cross-section of 2cm × 2cm at the front and 3cm × 3cm at the back; with its very low radiation length of 1.12 cm and Molière radius of 2.3 cm, at high energies up to 85% of the energy (depending on the impact point of the incident particle relative to the crystal centre) is deposited in the central crystal. This is in marked contrast with the shower caused by a hadronically interacting particle (we will return to this in detail later), as shown schematically in Figure 7.16. The fact that not all energy is deposited in the central crystal allows an estimate of the impact point of the incident particle. Like the energy resolution, the position resolution obtained this way improves as $E^{-1/2}$; at high energies, accuracies of about a mm have been obtained in the L3 detector.

- avalanche photodiodes or APDs, as used in the CMS experiment at the LHC. The APD oper-

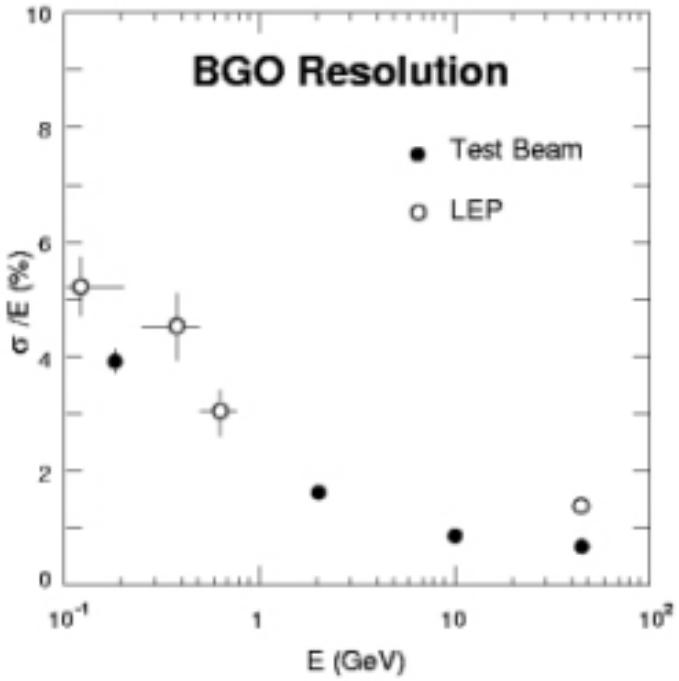

Figure 7.14: Resolution of the L3 EM calorimeter as a function of energy

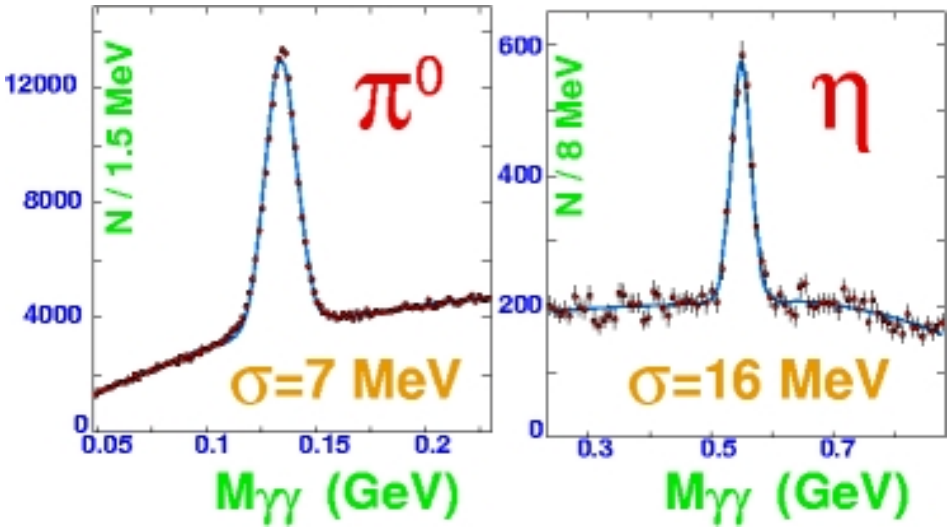

Figure 7.15: Reconstruction of π^0 and η mesons in the L3 EM calorimeter

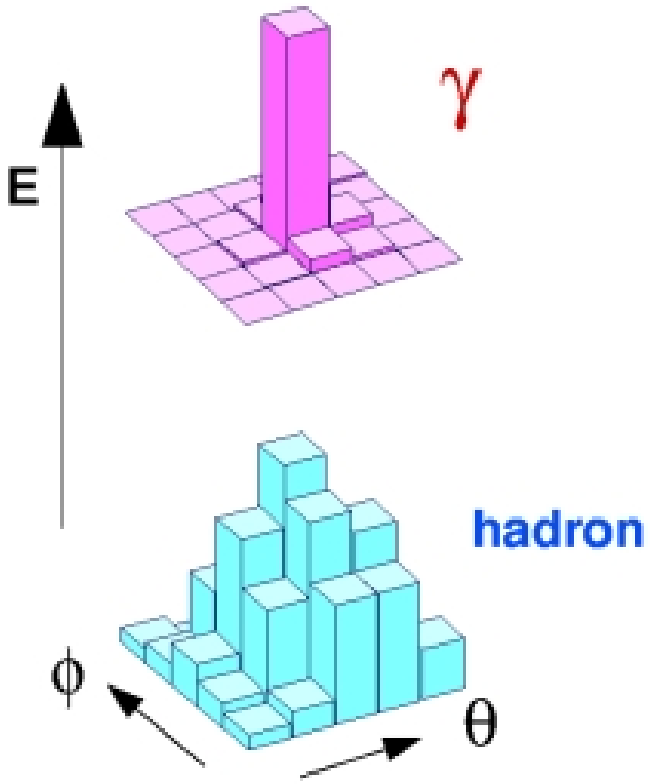

Figure 7.16: Transverse features of electromagnetic and hadronic showers in the L3 EM calorimeter

ating principle is shown in Figure 7.17. It largely resembles the "normal" photodiode, except

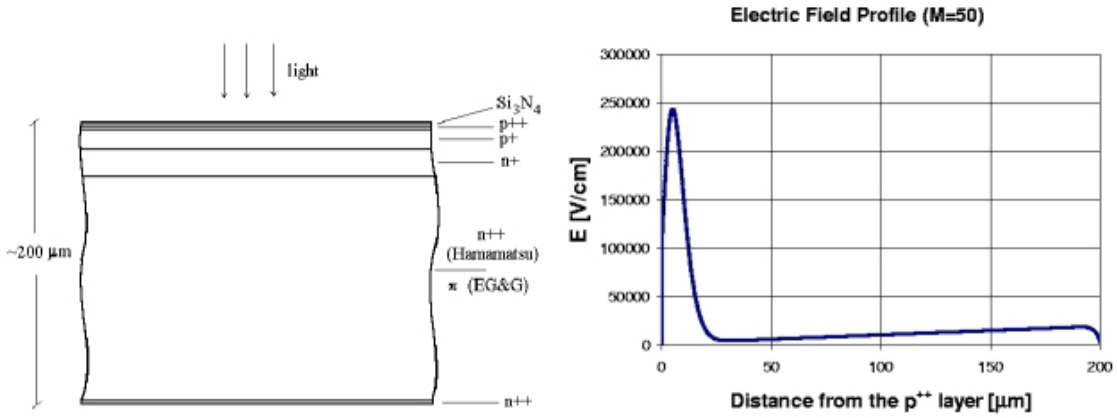

Figure 7.17: Operating principle of the APD developed for the CMS experiment

that there is a region in which, due to the doping profile, the electric field is sufficiently high to cause avalanche multiplication (by the electrons). The internal multiplication is necessary (in the case of the CMS experiment) to cope with the relatively low light yield of $PbWO_4$, ~ 50 photons per MeV of deposited energy. It is set by the applied bias voltage, with a goal of about 50.

An additional complication of using a device with internal amplification is that charged particles traversing the APD (hadrons or $e^{\pm}$ from longitudinal leakage) will create e-h pairs as well, and the amplification might lead to significant biases in the energy measurement. A great deal of attention has been spent verifying that this effect (called the *nuclear counter effect* in this context) will not be a serious problem.

In test beam setups, a stochastic contribution to the energy resolution of $4.3/\sqrt{E(\mathrm{GeV})}$ has been obtained. This resolution is somewhat worse than that obtained in the L3 experiment, but it has to be kept in mind that the aim of the CMS experiment is different: it attempts to achieve the best possible resolution for high-energy (of order 50 GeV or more) particles (notably, the search for the Higgs boson in its decay $H \to \gamma\gamma$), at which energies the resolution tends to be dominated by the constant term. The CMS detector will use about 77,000 crystals.

Cherenkov radiation

The use of Cherenkov radiation does not require a crystalline structure, and results in substantially cheaper (though less performant) solutions. One of the most often used ones is lead glass, PbO dissolved in glass. This material was used notably in the OPAL experiment at the CERN LEP collider. The lead glass used in this experiment's barrel electromagnetic calorimeter (the endcap calorimeter uses a slightly different material) has a high refractive index ($n \approx 1.85$ at $\lambda = 586$ nm), and a rather short radiation length of 1.50 cm. About 12,000 crystals were used in the OPAL EM calorimeter.

Due to the nature of the Cherenkov radiation mechanism, the light yield of lead glass is substantially lower than most of the scintillating crystals: of the order of several thousands of Cherenkov photons per GeV (not MeV!) of deposited energy. Due to this low light yield, internal amplification is necessary, and the OPAL collaboration resorted to using B-field tolerant PMTs for its barrel EM calorimeter (this was possible as this part of the calorimeter was located *outside* the solenoidal field

used for tracking, and only a modest stray field needed to be dealt with). In the case of the endcap calorimeter, the B field was substantial (0.4 T) and vacuum phototriodes (roughly, single-stage PMTs with a gain of about 10, depending only very weakly on the magnetic field) were used. A drawing of a vacuum phototriode is shown in Figure 7.18. The energy resolution obtained in crystals of about 10cm $\times$ 10cm cross-section was about $5\%/\sqrt{E(\mathrm{GeV})}$. Vacuum phototriodes will also be used for the readout of the endcap EM calorimeter of the CMS experiment: they are preferred over APDs due to their radiation-hardness. Another particularity of the use of Cherenkov radiation is that unlike scin-

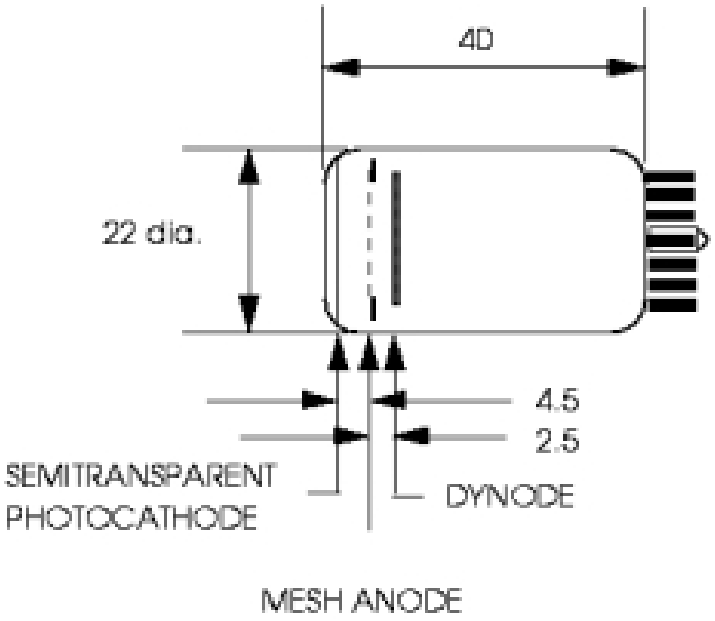

Figure 7.18: Drawing of a vacuum phototriode

tiallation, Cherenkov light is *directional*. The calorimeter response might therefore depend on the angle of incidence of the incoming particles. It was verified that in the case of the OPAL calorimeter, this was not a serious problem. (In any case, given the collider nature of most experiments there is a strong directional preference for perpendicular incidence.)

A photograph of (half of) the OPAL barrel EM calorimeter is shown in Figure 7.19.

Ionization

The use of ionization in *homogeneous* calorimeters is very rare, but one case is certainly worth mentioning: the calorimeter of the NA48 experiment at CERN. This detector uses the noble liquid krypton (customarily denoted as LKr, in this case at $T = 120$ K), which is sufficiently heavy ($Z = 36$) to have a rather short radiation length of 4.7 cm, a Molière radius of 6.1 cm. The average energy needed to create one electron-ion pair is 18.4 eV, *i.e.* somewhat lower than in the case of argon.

The goals of the NA48 experiment are very specific: produce a very accurate measurement of CP violation in the neutral kaon system. This topic deserves a much more description than is appropriate here; in the context of the present topic, it is sufficient to say that the experiment involves measuring the decays $\mathrm{K_L} \longrightarrow \pi^0\pi^0$ and $\mathrm{K_S} \longrightarrow \pi^0\pi^0$to a very high accuracy, about 0.1%. This requires a calorimeter with a very good energy resolution, a time resolution better than 500 ps (this requirement is due to the fact that the experiment uses very precise beam timing to indicate whether the particle

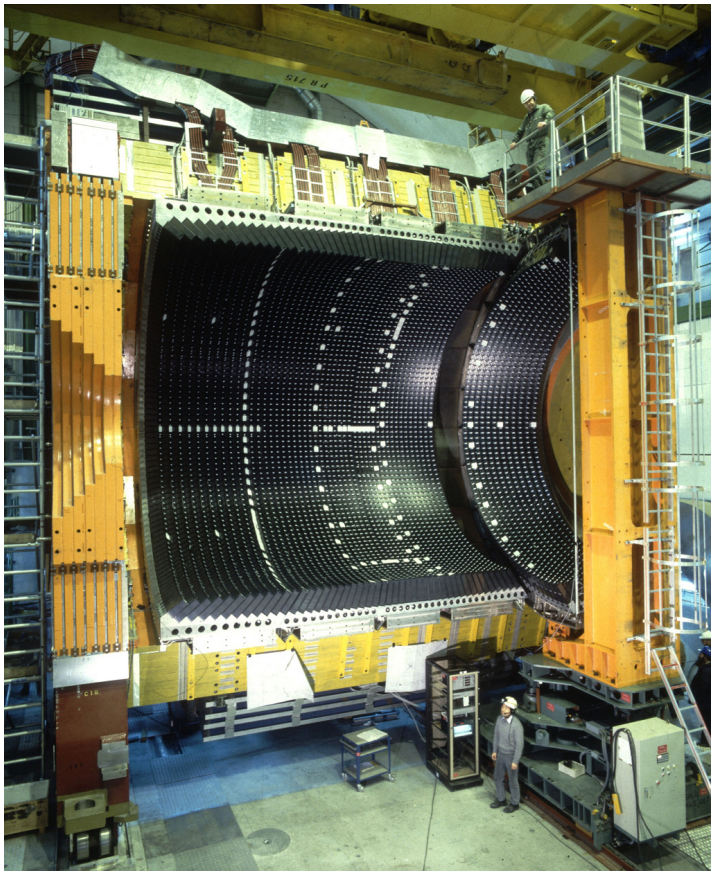

Figure 7.19: Photograph of the barrel of the OPAL EM calorimeter

that decayed to the di-pion state was a K_L or K_S), and very good stability over a period of years. In addition, the need to identify very efficiently the four photons involved in the above decays necessitates a not too high Molière radius.

The NA48 LKr calorimeter is shown schematically in Figure 7.20. As can be seen, the (very thin,

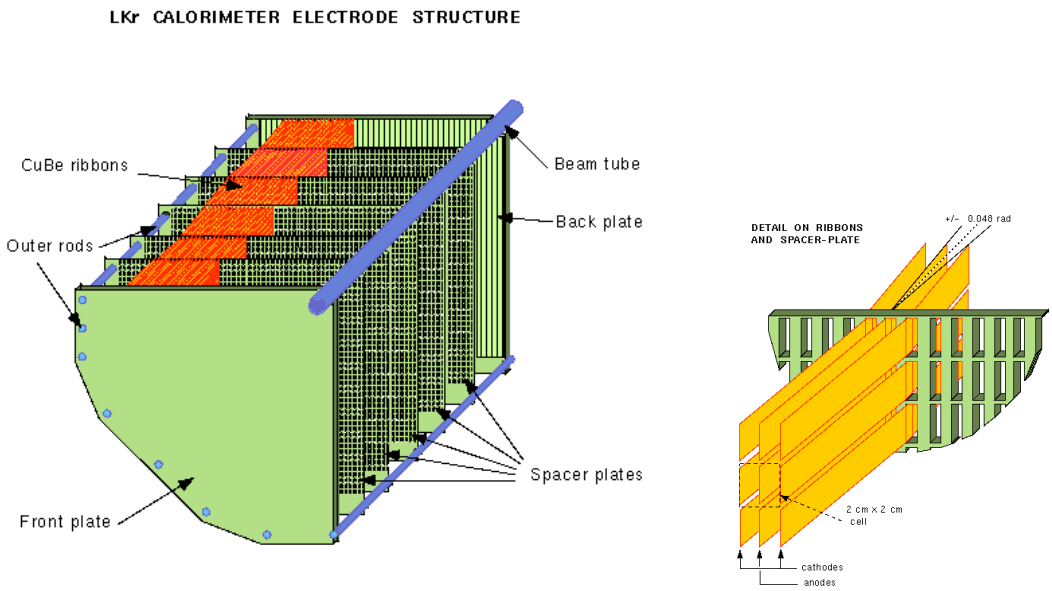

Figure 7.20: Schematic layout of the NA48 EM calorimeter

40 μm) copper-beryllium electrode structure is such that liberated electrons drift only small distances (up to 1 cm) to the anodes. To ensure a very good homogeneity, all electrodes are positioned to an accuracy better than 100 μm using spacers. The electrodes make an angle of 48 mrad with the beam direction in order to avoid a reduced response for photons incident at the positions of the electrodes.

The detector finally achieved an energy resolution characterized as

$$\frac{\sigma_E}{E} = \frac{3.2\%}{\sqrt{E}} \oplus 0.42\% \oplus 9\%/E,$$

with (as usual) E measured in GeV. The position resolution achieved was about 1 mm.

Sampling calorimeters

In sampling calorimeters, the two functions of a calorimeter (stopping high-energy particles, and measuring their energy) are fulfilled by different materials: a *passive* absorber medium and an *active* readout medium. This offers greatly increased flexibility compared to homogeneous calorimeters, in the sense that the passive and active media can be chosen separately: the absorber to have as high a value of Z as reasonably possible (uranium is the heaviest element that can be used), and the readout medium to ensure a high light yield, high speed, and/or good linearity.

Although the best energy resolution is typically achieved in homogeneous electromagnetic calorimeters, there can be good reasons to use sampling calorimeters instead:

- they are easy to machine and segment, and relatively cheap;

- they are intrinsically radiation hard (if a liquid or gaseous active medium is used, as this can be recirculated. In this case, also a good homogeneity is automatically obtained);

- they can be segmented longitudinally, and the ability to follow the longitudinal profile of a shower can help to distinguish between electromagnetic and hadronic showers, or to separate electromagnetic showers from nearby hadronic showers.

Analogously to homogeneous calorimeters, the observed signal in sampling calorimeters is determined by the energy that is lost in collisions in the active medium, by particles traversing this medium or ranging out in it. It follows that an important parameter is the *sampling fraction*: this is the fraction of the energy deposits by collision losses that occur in the active medium. More precisely, the definition is for collision losses by minimum ionizing particles. In homogeneous calorimeters, the difference with the energy loss by electrons and positrons can be neglected (as *all* energy is eventually deposited in the form of collision losses); however, in the case of sampling calorimeters many low-energy particles produced in the absorbers (especially towards the end of the shower) will not reach the active medium. This decreases the response to electrons relative to the response to MIPs. Nevertheless, the sampling fraction to first order is a useful indicator for the response to electrons.

An example is the calorimeter of the DØ experiment at the Tevatron. This calorimeter consists of 3 mm thick (depleted!) ^{238}U plates interleaved with 5 mm thick gaps filled with liquid argon (usually denoted as LAr). The total thickness amounts to 21 X_0 (the calorimeter already being preceded by material amounting to about 2 X_0, *e.g.* from the walls of the cryostat maintaining the LAr temperature at 80 K). For the readout, the calorimeter is divided longitudinally into four segments (of 2, 2, 7, and 10 X_0 depth). The transverse segmentation uses the *pseudorapidity* coordinate

$$\eta = -\ln\tan(\theta/2) \tag{7.5}$$

and is 0.1×0.1 in (ϕ, η) space; only at the third sample containing the shower maximum for high-energy showers, the segmentation is finer, 0.05×0.05, in order to obtain a more precise position reconstruction as well as an improved electron-hadron separation. This calorimeter is schematically shown in Figure 7.21 (the EM calorimeter is followed immediately by the hadronic calorimeter, in the same cryostat; only the yellow regions in the left Figure are part of the EM calorimeter).

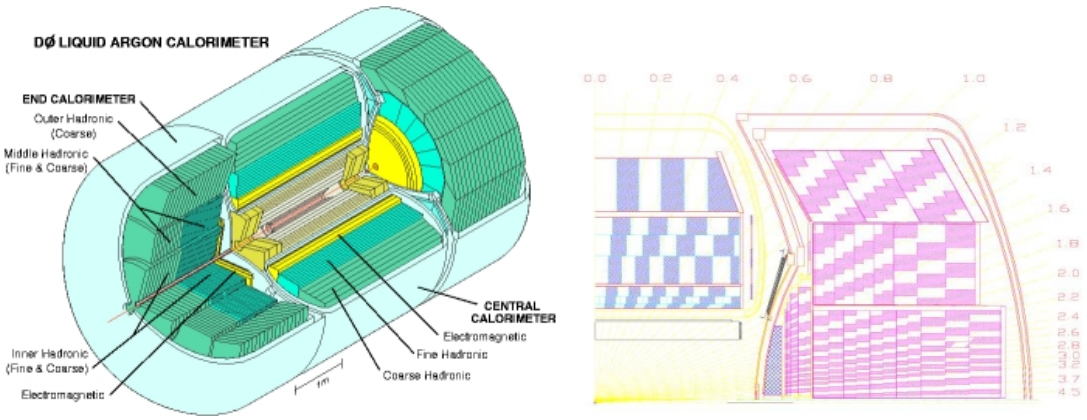

Figure 7.21: Schematic layout of the DØ calorimeter, and its segmentation

The sampling fraction f can be computed from the energy loss for a MIP (20.5 MeV/cm in the

uranium and 2.13 MeV/cm in the LAr):

$$f = \frac{0.5\text{cm} \cdot 2.13\text{MeV/cm}}{0.3\text{cm} \cdot 20.5\text{MeV/cm} + 0.5\text{cm} \cdot 2.13\text{MeV/cm}} \approx 0.15.$$

With an average of 26 eV to create one electron-ion pair, the average response to electrons is about $6 \cdot 10^6 e^-$/GeV, comparable to the yield in *e.g.* BGO.

The drift electrons liberated in the LAr drift towards anodes located in the middle of the drift gap, deposited as a resistive epoxy onto a G10 (fibre glass) support held in position using spacers. The applied voltage across a gap of 2.3 mm is 2 kV; the resulting electric field ($8.7 \cdot 10^3$V/cm) is high enough that the drift velocity saturates, at a value of 5 μm/ns, leading to a maximum drift time of ~ 450 ns. This is well below the bunch spacing used in Run I of the Tevatron (3.6 μs), though somewhat long for operation in the present Run II (396 ns). The drift velocity is sufficiently low that no avalanche multiplication takes place.

The energy resolution of sampling calorimeters, compared to homogeneous calorimeters, is usually described in terms of *sampling fluctuations* [6]: in the approximation that the collision losses due to MIPs and low-energy $e^\pm$ are similar, Rossi's "Approximation B" posits that the combined track length of all electrons and positrons will be equal to that of a MIP of energy E of the incoming particle. The effective number of shower particles crossing the active media is then equal to

$$N = E/\Delta\varepsilon,$$

where $\Delta\varepsilon$ is the average energy lost by a MIP in one sampling layer. This number of shower particles then follows a Poisson distribution, leading to a typical $1/\sqrt{E}$ stochastic contribution to the resolution. The situation is slightly more complex in the sense that Approximation B neglects the finite angles of the shower particles with respect to the shower axis. This can be incorporated as a change in the effective value of $\Delta\varepsilon$, dividing it by the cosine of the track angle. With the parametrisation of the average cosine (obtained from detailed MC computations),

$$\langle \cos\theta \rangle \approx \cos(E_s/\pi E_c),$$

the resolution can be parametrised as

$$\frac{\sigma_E}{E} = \left(\frac{\Delta\varepsilon(\text{MeV})}{\cos(E_s/\pi E_c)} \right)^{1/2} \cdot \frac{3.2\%}{\sqrt{E(\text{GeV})}}.$$

Note that the validity of this formula is limited to sampling fractions that are not very small. For small sampling fractions, other effects that become significant are:

- *path length fluctuations*: the angular spread of low-energy shower particles is significant, and multiple scattering into the active plane may increase their "visible" path length even more. This effect is less important in dense readout media as the ranges of low-energy particles become comparable to the thickness of the active layers;
- *Landau fluctuations*: as discussed in Chapter 3, the distribution of the energy loss of charged particles in thin layers of material develops an asymmetric tail, and the resulting distribution is known as the *Landau distribution*. The resulting contribution to the energy resolution has been given as [7]

$$\frac{\sigma_E}{E} \approx \frac{3}{\sqrt{N} \cdot \ln(1.3 \cdot 10^4 \Delta\varepsilon)}.$$

These two effects are usually significant only for detectors with gaseous readout media (*e.g.* in the form of proportional tubes); an exception is the use of silicon sensors as the readout medium, interleaved with tungsten absorbers, in the luminosity monitors of *e.g.* the ALEPH and OPAL experiments at LEP.

Finally, it should be pointed out that care should be taken to ensure that the response of the readout medium is linear: this is relevant in particular for detectors using (organic) scintillator readout.

The energy resolution achieved using the DØ EM calorimeter in Run I was

$$\frac{\sigma_E}{E} = \frac{16\%}{\sqrt{E}} \oplus 0.3\% \oplus \frac{0.3}{\text{GeV}}.$$

7.2 Hadronic Calorimetry

While the energy degradation in an EM shower involves only two well-understood processes, the situation for hadronic calorimetry is substantially more complicated. Hadronic calorimetry refers to the absorption and measurement of hadrons: primarily these are protons, (charged) pions, and kaons (other hadrons typically having decayed before reaching the calorimeter). These hadrons will also encounter EM interactions with the calorimeter's atomic nuclei and electrons (in case they are charged); however, strong interactions with the nuclei are now important as well.

7.2.1 Hadronic interactions

The first nuclear interaction (neglecting soft elastic collisions) is one in which the incident hadron interacts inelastically with one nucleon. In this primary process, depending on its centre-of-mass energy (which depends on the energy of the incoming particle and the mass of the target nucleus as $\sqrt{2Em}$), tens of charged and neutral particles, predominantly pions, can be produced; these *secondaries* have transverse momenta (with respect to the direction of the incident hadron) of the order of 350 MeV. However, the nucleon is not a free particle, and a significant fraction of the incident hadron's energy can also be spent on the excitation or spallation of the nucleus.

An important quantity in the context of hadronic showers is the *nuclear interaction length* λ_{int}: the probability for a particle traveling with a certain energy not to have undergone an inelastic interaction is given by

$$P(x) = e^{-x/\lambda_{\text{int}}}.$$

As usual, the interaction length is related to the total nuclear interaction cross section through

$$\lambda_{\text{int}} = \frac{A}{n_A \sigma_{\text{tot}}}.$$

A rough dependence of the cross section on A is easily derived from a geometric argument: the geometric cross section scales as $A^{2/3}$. Expressed in units of gcm^{-2}, λ_{int} therefore scales as $A^{1/3}$: experimentally, $\lambda_{\text{int}} \approx 35A^{1/3}$ for protons, and about two thirds of that for pions (which themselves are smaller). For sufficiently high energy, λ_{int} becomes nearly independent of energy.

Hadronic calorimeters are typically 8-10 λ_{int} thick (depending on the energies of incident hadrons) in order to contain fully the hadronic showers. It is also useful to point out that for not too light elements, the interaction length greatly exceeds the radiation length. Often used examples are Fe ($\lambda_{\text{int}} = 132\text{gcm}^{-2}$, $X_0 = 13.8\text{gcm}^{-2}$), Cu ($\lambda_{\text{int}} = 135\text{gcm}^{-2}$, $X_0 = 12.9\text{gcm}^{-2}$), Pb ($\lambda_{\text{int}} = 194\text{gcm}^{-2}$, $X_0 = 6.4\text{gcm}^{-2}$), and U ($\lambda_{\text{int}} = 199\text{gcm}^{-2}$, $X_0 = 6.0\text{gcm}^{-2}$). It is this difference which makes it possible to separate calorimetry into electromagnetic and hadronic calorimetry: a full EM calorimeter usually

represents "only" 1-2 λ_{int}, so that many hadrons will simply traverse the EM calorimeter and leave a MIP signal (in the case of charged hadrons). Still, many hadrons will encounter a nuclear interaction in the EM calorimeter of an experiment, and care has to be taken to recognize these as such and provide an accurate energy reconstruction.

One of the most salient features of hadronic showers is the increase of the EM component with energy. The origin of this effect is easily understood qualitatively: most of the long-lived particles emerging from a high-energy hadronic interaction are pions, with an average fraction of π^0, f_{π^0}, of about 1/3. Due to its decay $\pi^0 \longrightarrow \gamma\gamma$, the production of π^0 therefore converts a sizeable fraction of the hadronic shower into an EM one. That the EM fraction increases with energy is also easy to see, from the fact that the hadrons remaining after one stage of the shower may encounter new interactions, in which again π^0 are produced. The EM fraction can be parametrised as

$$f_{\text{EM}} = 1 - (E/E_0)^{k-1}\,, \tag{7.6}$$

where E_0 is a scale factor corresponding roughly to the average energy needed to create one pion, and k is related to the average multiplicity $\langle m \rangle$ (assumed independent of E) and to f_{π^0} by

$$k - 1 = \frac{\ln(1 - f_{\pi^0})}{\ln\langle m \rangle}$$

This number depends only weakly on the average multiplicity (which in reality has a logarithmic dependence on the centre-of-mass energy), and is approximately equal to 0.8.

It turns out that Eqn. 7.6 does give a reasonable description of the experimental data, if the values of E_0 and k are chosen appropriately. In particular, the value of E_0 increases with Z (from 0.7 for Cu to 1.3 for Pb), leading to lower EM fractions. Moreover, proton induced showers lead to an EM fraction about 15% lower than pion induced showers, a fact which is easily explained by the fact that the cascade described above does not account correctly for baryon number conservation: unlike for mesons, no decays are possible by which baryons disappear.

Besides the high energy shower, other processes also occur:

- ionization energy loss: many of the particles produced in the cascade are quite soft (energies of a few hundred MeV), and they lose a lot of their energy through ionization;
- spallation reaction: in the de-excitation (or break-up) process occurring after the collision with the high energy hadron, hundreds of different final states (for high values of Z of the absorber) may be formed. In general, a substantial number of nucleons (mostly neutrons, but sometimes also heavy fragments of the nucleus like α) are "evaporated". In order for the evaporation process to take place, a fraction of the high energy hadron's energy must be used to overcome the nucleus's binding energy;
- charge exchange processes: in particular, the reaction $\pi^+\text{n} \rightarrow \pi^0\text{p}$ leads to large fluctuations, as almost the full energy of the incoming pion is converted to EM energy (again through the decay $\pi^0 \rightarrow \gamma\gamma$).

7.2.2 Response

As in the case of EM calorimeters, the observed signal in hadronic calorimeters is due to ionization, scintillation, or Cherenkov radiation. Invariably, sampling calorimeters are used in hadronic calorimetry. Of great importance is the *response* of the calorimeter. Denoting the response to a particle by the

particle itself, this is typically written as

$$\pi = f_{\mathrm{EM}} e + (1 - f_{\mathrm{EM}}) h \Rightarrow e/\pi = \frac{e/h}{1 - f_{\mathrm{EM}}(1 - e/h)}. \tag{7.7}$$

Here, e and h are the response to the EM and hadronic parts of the shower, respectively. It can be seen from Eqn. 7.7 that unless $e/h = 1$, the fact that f_{EM} grows with energy will introduce a nonlinearity in the response. In addition, the fluctuations in f_{EM} from shower to shower lead to an increased energy resolution.

It is therefore important to consider in more detail the term e/h. From the above discussion we find that this term can be written as

$$e/h = \frac{e/\mathrm{mip}}{f_{\mathrm{rel}}\mathrm{rel/mip} + f_{\mathrm{p}}\mathrm{p/mip} + f_{\mathrm{n}}\mathrm{n/mip} + f_{\mathrm{inv}} \cdot 0/mip},$$

where

- “mip” denotes minimum ionizing particles, *e.g.* muons
- “rel” denotes relativistic hadrons, *i.e.* mainly charged pions, which deposit their energy through ionization;
- “p” denotes the spallation protons, which similarly deposit their energy through ionization;
- “n” denotes the evaporation neutrons;
- and “inv” denotes nuclear excitation and recoil, which do not contribute to the signal.

For the individual terms, we have:

- e/mip < 1: many of the generated $e^{\pm}$ in EM showers are soft, with energies < 1MeV. These particles have a large probability to be stopped in the absorber, depending on the sampling fraction;
- rel/mip $= 1$, perhaps with slight modifications due to the energy dependence of collision losses;
- p/mip: this is again more complicated, as even though the energy loss mechanism is again ionization, the low energies again lead to a high probability that the protons will range out in the absorber. The absorber thickness is again an important parameter;
- n/mip: this term depends on the interactions encountered by neutrons: nuclear reactions like (n,α), excitation of nuclei, and elastic scattering. In practice, most energy is lost in elastic scattering, particularly in hydrogen rich materials such as plastic scintillators. In addition, a very special case is that of ^{238}U, in which fission can be induced by slow neutrons, leading to detectable energy and thus increasing the response to neutrons.

On the basis of the above, it is in principle possible to construct a calorimeter with $e/h = 1$, also called a *compensating* calorimeter (note that in part, this relies on having e/mip < 1, and therefore this cannot be achieved in homogeneous calorimeters).

A compensating calorimeter has been built notably by the ZEUS collaboration at the HERA e-p collider at DESY, Hamburg. This detector has indeed achieved $e/h = 1$ for hadron energies above 3 GeV, using a uranium-scintillator sandwich structure. A photograph is shown in Figure 7.22.

Figure 7.22: Uranium-scintillator structure of the ZEUS calorimeter

As a result of its good e/h ratio, the energy resolution of this calorimeter was exceptionally good: $\sigma_E/E = 0.35/\sqrt{E}$, to be compared with a moderate EM resolution of $\sigma_E/E = 0.18/\sqrt{E}$. This hadronic energy resolution is significantly better than can be expected in detectors where compensation has not been addressed specifically. In typical hadron calorimeters, where $e/h \approx 1.4$, one finds an intrinsic energy resolution of $\sigma_E/E \approx 0.45/\sqrt{E}$. The calorimeter of the DØ experiment, despite its being nearly compensating ($e/h \approx 1.08$), was able to achieve $\sigma_E/E = 0.45/\sqrt{E}$ at best.

Finally, it has to be kept in mind that in a colliding beam experiment, one is usually interested not so much in the energy resolution of individual hadrons, but rather in that of the jet that the hadrons are part of (since the jet is the result of the fragmentation of a quark, anti-quark, or gluon, and it is often these partons which of primary interest). However, from the perspective of a calorimeter measurement, a jet is little more than a collection of hadrons (and photons from the decay of π^0 produced in the physics interaction). Therefore, the energy resolution follows roughly that of individual hadrons. The angular resolution for jets is tyically of the order of 10-50 mrad, improving with energy.

Bibliography

[1] R. Wigmans, Calorimetry, (Oxford Science Publications, 2000), ISBN 0-19-850296-6

[2] J.D. Jackson, Classical Electrodynamics, (Wiley, 1975), ISBN 0-471-43132-X

[3] Y-S. Tsai, Rev. Mod. Phys. **46** (1974) 815

[4] S. Eidelman *et al.,* Physics Letters **B592** (2004) 1

[5] B. Rossi, High-Energy Particles, (Prentice-Hall, 1953)

[6] U. Amaldi, Physica Scripta **23** (1981) 409, reprinted in *Experimental Techniques in High Energy Physics*, ed. T. Ferbel, 1987

[7] C. Fabjan, *Calorimetry in High Energy Physics*, Addison-Wesley, 1987, ISBN 0-201-11487-9